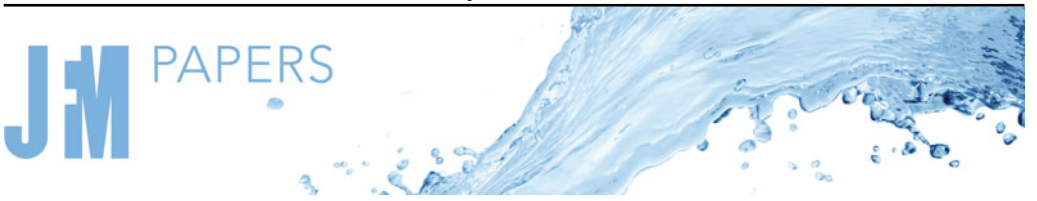
J. Fluid Mech. (2026), *vol.* 1039, A34, doi:10.1017/jfm.2026.11842



On the Reynolds analogy for high-speed rough-wall flows: implications for wall modelling

Michele Cogo[1,2], **Davide Depieri**[3], **Matteo Bernardini**[2] and **Francesco Picano**[1,3]

[1]Department of Industrial Engineering, Università degli Studi di Padova, via Venezia 1, 35131 Padova, Italy

[2]Department of Mechanical and Aerospace Engineering, Sapienza University of Rome, via Eudossiana 18, 00184 Rome, Italy

[3]CISAS 'Giuseppe Colombo', Università degli Studi di Padova, via Venezia 1, 35131 Padova, Italy

Corresponding author: Michele Cogo, michele.cogo@unipd.it

(Received 23 December 2025 UTC; revised 16 June 2026 UTC; accepted 22 June 2026 UTC)

We investigate compressible turbulent boundary layers over prism-shaped roughness using direct numerical simulations at Mach 2 and 4, with adiabatic and isothermal walls. Analysis of instantaneous and mean-density fields shows that compressibility effects and wall-thermal conditions significantly influence the boundary-layer structure, although the roughness elements remain submerged within the subsonic layer. While roughness disrupts near-wall momentum–energy coupling within the roughness sublayer, the Reynolds analogy recovers in the outer region where velocity and temperature fields exhibit smooth-wall-like similarity. A systematic comparison of different formulations indicates that a mixed Prandtl number approach provides the most accurate heat-flux predictions among the tested closures. Based on these observations, we develop a wall model that couples drag prediction for small prism-shaped roughness patterns with a compressibility transformation and a temperature–velocity closure. The formulation is modular, allowing the straightforward incorporation of alternative closures and traditional correlations. The model predicts both wall-shear stress and heat flux using only roughness geometry and information from the matching location, and shows good *a priori* agreement with the present direct numerical simulation data.

Key words: compressible boundary layers, turbulent boundary layers, supersonic flow

© The Author(s), 2026. Published by Cambridge University Press. This is an Open Access article, distributed under the terms of the Creative Commons Attribution licence (https://creativecommons.org/licenses/by/4.0/), which permits unrestricted re-use, distribution and reproduction, provided the original article is properly cited.

https://doi.org/10.1017/jfm.2026.11842 Published online by Cambridge University Press

1. Introduction

The interaction between compressibility, surface roughness and heat transfer poses a longstanding challenge in the understanding and modelling of wall-bounded high-speed flows. These effects are central to many high-speed applications and directly impact drag and heat transfer, which are critical to the structural integrity of vehicles operating in and out of the atmosphere. In particular, the accurate prediction of thermal loads is inherently tied to our ability to assess the relation between velocity and temperature fields, which are nonlinearly coupled through density. However, surface roughness further complicates this coupling, and our predictive capabilities for such flows still rely heavily on semi-empirical correlations that do not generalise across the vast parameter space spanned by Mach number, wall-thermal conditions and roughness geometries (Bowersox 2007).

In smooth-wall compressible boundary layers (BLs), mean thermodynamic quantities are related to the mean momentum field through the Reynolds analogy, independently formulated by Busemann (1931) and Crocco (1932) under the assumption of unit Prandtl number ($Pr = 1$). Under this hypothesis, the mean temperature $\bar{T}$ becomes a quadratic function of the mean streamwise velocity $\bar{u}$, establishing a direct and remarkably simple connection between temperature and momentum fields.

The assumption $Pr = 1$ is central to the original derivation, as it implies identical molecular diffusivities of momentum and heat. However, real gases typically exhibit $Pr \neq 1$, and turbulent flows introduce an additional turbulent Prandtl number Pr_t, reflecting the relative efficiency of turbulent momentum and heat transport. Deviations from unity, both at the molecular and turbulent levels, therefore, play a crucial role in determining the validity and accuracy of Reynolds-analogy-based relations.

Subsequent studies introduced progressively refined corrections accounting for non-unity Prandtl number, wall heat transfer and more complex boundary conditions (Walz 1969; Huang & Coleman 1994; Zhang *et al.* 2014). These developments retained the quadratic temperature–velocity structure while modifying the coefficients to reflect realistic transport properties. A particularly systematic formulation is the generalised Reynolds analogy (GRA) proposed by Zhang *et al.* (2014). Rather than prescribing a specific recovery factor r, the GRA introduces a generalised version, r_g, which incorporates Mach number and wall temperature effects.

The GRA has been assessed against an extensive set of direct numerical simulation (DNS) databases, including compressible channel flows, pipe flows and BLs with both adiabatic and cooled walls (Cogo *et al.* 2023), and has proven highly effective in rationalising smooth-wall compressible turbulence. Additionally, it serves as a general theoretical framework within which different modelling assumptions, including earlier formulations of Walz (1969) or Huang & Coleman (1994), can be interpreted and systematically compared.

From an engineering standpoint, one of the most important observations of the extensive work dedicated to the Reynolds analogy is the universality of the Reynolds analogy factor $s = 2C_h/C_f$, which is shown to hold approximately constant when coupled with the Prandtl number ($sPr \approx 0.8$), with weak dependence on the Mach number and wall temperature condition (Zhang *et al.* 2014; Cogo *et al.* 2023). Here, $C_f = 2\tau_w/(\rho_\infty u_\infty^2)$ is the skin friction coefficient and $C_h = q_w/(\rho_\infty u_\infty c_p(T_w - T_r))$ is the Stanton number, whose relation through s has far-reaching implications for reduced-order modelling, given that it directly relates the wall-shear stress τ_w and heat transfer q_w, where u_∞ is the freestream velocity, ρ_∞ is the freestream density, and c_p is the heat capacity at constant pressure.

In this context, it is well known that the presence of surface roughness clearly affects the value of s (Hill, Voisinet & Wagner 1980; Modesti *et al.* 2022), being usually lower than

https://doi.org/10.1017/jfm.2026.11842 Published online by Cambridge University Press

the reference smooth-wall case. The general consensus is that the increase in skin friction caused by roughness is greater than the corresponding increase in heat transfer. This is because the additional wall-shear stress is transmitted to the surface as a form drag on the individual asperities, while the heat flux is only controlled by the thermal conductivity (Owen & Thomson 1963). Several studies have been conducted to account for this effect with semi-empirical relations (Owen & Thomson 1963; Chen 1972; Hill *et al.* 1980), which nevertheless suffer from poor generalisability.

Notwithstanding the additional layer of complexity added by rough surfaces, it is important to note that s can be interpreted as an integral measure of the Reynolds analogy (RA) (Wenzel, Gibis & Kloker 2022), and in this sense its departure from universality for rough-wall flows does not directly imply that the analogy between averaged momentum and energy equations is invalid locally everywhere in the flow.

The present study aims to build on this consideration by assessing the validity of the RA throughout the entirety of the BL, which has important implications for the prediction of the wall heat transfer for compressible flows over rough walls. To this end, we leverage a novel DNS dataset of compressible turbulent BLs over prism-shaped roughness based on the works of Cogo *et al.* (2025*a*,*b*), encompassing Mach numbers 2 and 4 and two wall temperature conditions: adiabatic and cold wall. Building on our findings, we propose a wall model for compressible rough-wall flows by extending the drag-predictive method introduced by Yang *et al.* (2016) for incompressible flows, which explicitly accounts for the sheltering mechanism induced by prism-shaped roughness.

2. Computational set-up

The present study is based on a novel dataset of DNSs of supersonic, zero-pressure-gradient, turbulent BL at free-stream Mach numbers of $M_\infty = 2$ and $M_\infty = 4$, over cubical, aligned roughness elements. For each Mach number, we conduct one simulation at adiabatic conditions $\partial T/\partial y = 0$ (or $\Theta = (T_w - T_\infty)/(T_r - T_\infty) \approx 1$ where $T_r = T_\infty + r(\gamma - 1)M_\infty^2/2$ is the recovery temperature and $r = Pr^{1/3}$ is the recovery factor), where γ is the speific heat ratio and cold wall isothermal conditions $\Theta = 0.25$, for a total of four cases. In the present database, the use of the diabatic parameter Θ is adopted given its capability to recover the same behaviour in terms of wall cooling across different Mach numbers (Cogo *et al.* 2023).

Throughout the manuscript, the four supersonic rough-wall boundary-layer cases are denoted as M2A, M2I, M4A and M4I, indicating the two Mach numbers considered and the wall-thermal condition, either adiabatic (A) or isothermal (I) (see table 2).

All rough cases in the present study feature the same roughness pattern, which is shared with the previous work of Cogo *et al.* (2025*a*) and case CB_A of Cogo *et al.* (2025*b*). This pattern consists of cubical elements of equal size k equally spaced in the streamwise and spanwise directions by a length of $2k$. Compared with the inflow boundary-layer thickness δ_{in}, the roughness height is $k = 0.12\,\delta_{in}$. All DNS calculations are carried out using STREAmS (Bernardini *et al.* 2023; Sathyanarayana *et al.* 2025), an open source numerical solver orientated to modern high-performance-computing platforms using message-passing-interface parallelisation and supporting multi-GPU architectures. We solve the compressible Navier–Stokes equations for a viscous, heat-conducting gas, where molecular viscosity μ is assumed to follow Sutherland's law, with a reference free-stream temperature $T_\infty = 220$ K. The thermal conductivity $\lambda = \mu c_p/Pr$ is related to the viscosity through the Prandtl number $Pr = 0.72$. Convective terms are discretised using sixth-order, energy-preserving schemes in shock-free regions, while a high-order

https://doi.org/10.1017/jfm.2026.11842 Published online by Cambridge University Press

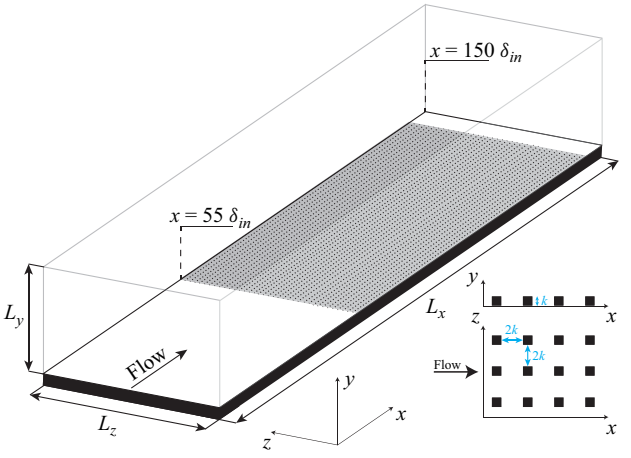


Figure 1. Schematic of the computational domain (not to scale), featuring an initial smooth surface followed by a rough region. The roughness pattern consists of three-dimensional wall-mounted cubical elements of height k and spacing $2k$.

shock-capturing scheme weighted essentially non-oscillatory (WENO) is activated in the presence of shock waves, as identified by the Ducros sensor (Ducros *et al.* 1999). Viscous terms are discretised using a locally conservative formulation (De Vanna *et al.* 2021) with sixth-order accuracy. The system of equations is completed by the equation of state for a calorically perfect gas and is solved on a Cartesian grid using a ghost-point-forcing immersed boundary method (IBM) to handle the complexity of the geometry. This method has been extensively validated for roughness in previous works by the same group (Cogo *et al.* 2025*a*,*b*). According to Chaudhuri *et al.* (2011), when combined with shock-capturing schemes and a fifth-order WENO discretisation, the IBM exhibits second-order accuracy in the vicinity of solid boundaries. The computational domain consists of a smooth-wall inflow region used to generate a fully turbulent BL of initial thickness δ_{in} via a recycling–rescaling procedure, followed downstream by a rough-wall region starting from $x = 55\,\delta_{in}$, where prism-shaped roughness elements are embedded, see figure 1. The domain extends $L_x \times L_y \times L_z = 150 \times 25 \times 8.28\,\delta_{in}$, with the recycling plane at $x = 40\,\delta_{in}$, the rough region spanning $55 \leqslant x/\delta_{in} \leqslant 147$ and a short smooth-wall buffer before the outflow. Non-reflecting boundary conditions based on characteristic decomposition are imposed at the upper and outflow boundaries. The spanwise boundary condition is periodic and implemented with the same formal accuracy as the interior scheme. The spanwise domain accommodates 23 repetitive roughness units (each of width $3k$), ensuring that the periodic boundary condition does not artificially constrain the turbulent structures in the spanwise direction and that statistical homogeneity is well preserved.

All simulations share the same grid resolution, composed of $20240 \times 556 \times 1408$ points in the streamwise, wall-normal and spanwise directions, respectively. The spanwise grid spacing is uniform throughout the domain. In the streamwise direction, a coarser spacing is used in the smooth inflow region and gradually refined towards the rough-wall region, with a streamwise refinement ratio of 2.5. In the wall-normal direction, approximately 40 grid points are distributed within the roughness height k, with nearly uniform spacing up to the roughness crest; the mesh is then progressively coarsened through the BL up

https://doi.org/10.1017/jfm.2026.11842 Published online by Cambridge University Press

Case	Station	Δx^+	Δz^+	Δy_w^+	Δy_k^+	Δy_δ^+	δ_{99}/δ_{in}	Re_τ	Re_θ
M2A	$x/\delta_{in}=50$	2.6	2.3	0.4	—	5.1	1.8	694	3314
	$x/\delta_{in}=127$	2.8	2.8	0.5	2.4	7.2	3.4	1574	7259
M2I	$x/\delta_{in}=50$	2.5	2.2	0.4	—	5.0	1.9	698	2196
	$x/\delta_{in}=127$	2.7	2.7	0.5	2.3	7.0	3.5	1588	4905
M4A	$x/\delta_{in}=50$	2.7	2.3	0.4	—	5.2	1.7	685	6727
	$x/\delta_{in}=127$	3.0	3.0	0.5	2.5	7.7	3.4	1650	14119
M4I	$x/\delta_{in}=50$	2.4	2.1	0.4	—	4.8	1.8	660	2907
	$x/\delta_{in}=127$	2.5	2.5	0.4	2.1	6.5	3.6	1508	6326

Table 1. Grid resolution and boundary-layer properties at selected smooth and rough streamwise stations for each DNS case. Here, Δx^+ and Δz^+ are the streamwise and spanwise grid spacings in wall units, Δy_w^+ is the wall-normal spacing at the bottom wall, Δy_k^+ at the roughness crest and Δy_δ^+ at the boundary-layer edge. Here, $Re_\theta = \rho_\infty u_\infty \theta/\mu_\infty$, where θ is the momentum thickness.

Colour	Case	M_∞	$\bar{M}_k$	Surface	Θ	T_w/T_r	Re_τ	δ_{99}/k	k^+
	M03 (Cogo *et al.* 2025*a*)	0.3	—	Cubical	1.0	1.0	1600	28.5	56
	M2A (Cogo *et al.* 2025*a*)	2	0.36	Cubical	1.0	1.0	1574	27.7	57
	M2I	2	0.4	Cubical	0.25	0.69	1588	28.9	55
	M4A	4	0.54	Cubical	1.0	1.0	1650	27.6	60
	M4I	4	0.6	Cubical	0.25	0.44	1508	29.9	51

Table 2. Summary of parameters for DNS study at selected station, $x = 127\delta_{in}$. Here, $\Theta = (T_w - T_\infty)/(T_r - T_\infty)$ is the diabatic parameter, T_w/T_r the wall-to-recovery temperature ratio, $Re_\tau = \rho_w u_\tau \delta_{99}/\mu_w$ the friction Reynolds number, k the roughness height and $\bar{M}_k$ the averaged Mach number at the roughness crest. The boundary-layer thickness δ_{99} is computed using the location where $\bar{u}/u_\infty = 0.99$.

to $y \approx 3.8\,\delta_{in}$ (local stretching ratio ≈ 8), beyond which a stronger stretching (local ratio ≈ 20) is applied up to the top of the domain.

The local grid resolution in wall units at representative smooth- and rough-wall streamwise stations is reported in table 1, together with key boundary-layer properties. From this table it is evident that the resolution requirements imposed by the need to accurately resolve the roughness elements are more demanding than those dictated by the turbulent flow alone, and that the present simulations are well within DNS quality standards for all cases.

Reynolds averages are computed by combining averaging in the spanwise direction, temporal averaging over at least 500 δ_{in}/u_∞ and averaging over a short streamwise window of four roughness wavelengths. Below the roughness crest, an intrinsic (fluid-only) spatial average is applied. Resources for one simulation consisted of 64 nodes with 4 x GPUs/node (256 GPUs in total) for a domain discretised with approximately 16 billion nodes and it was computed by the Leonardo cluster at CINECA. All four cases have been sampled at the streamwise station $x/\delta_{in} = 127$, ensuring an acceptable adjustment of the flow to the rough surface after the smooth-to-rough transition, and related properties are reported in table 2, including the friction Reynolds number Re_τ, the ratio k/δ_{99} and the roughness Reynolds number k^+.

https://doi.org/10.1017/jfm.2026.11842 Published online by Cambridge University Press

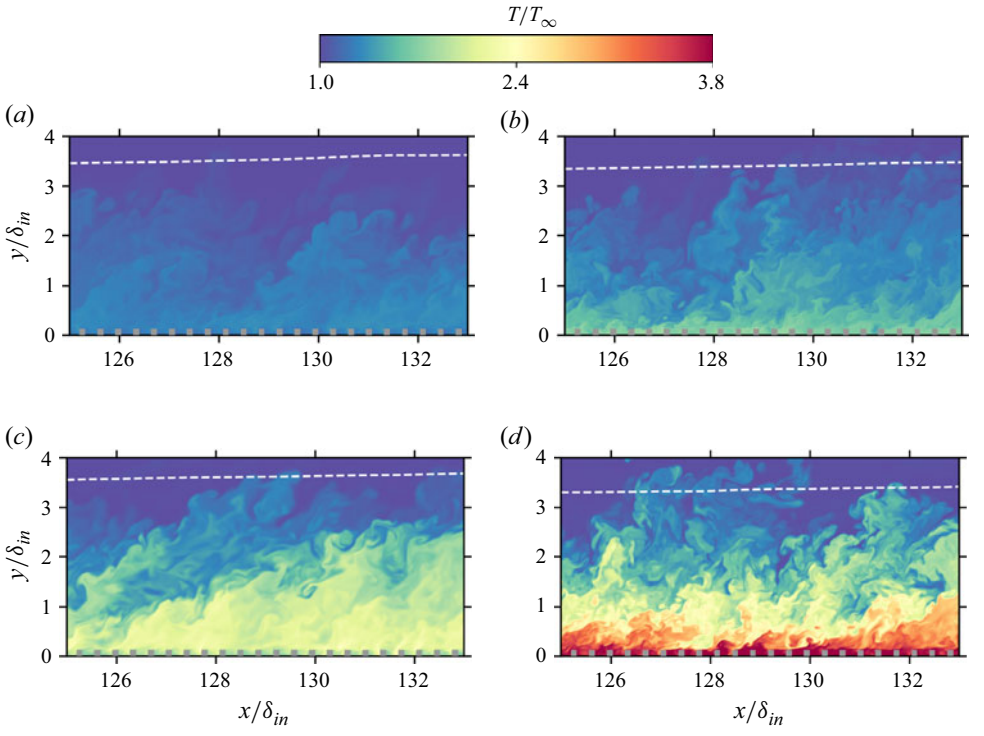


Figure 2. Instantaneous temperature field T/T_∞ visualised in an x–y slice bisecting half the roughness elements. Panels show cases (*a*) M2I, (*b*) M2A, (*c*) M4I, (*d*) M4A. The white dashed line denotes the average location of the boundary-layer thickness δ_{99}.

3. Database overview

3.1. *Instantaneous and mean flow fields*

To provide a qualitative overview of the interaction between the mean flow dynamics and the roughness elements, figure 2 shows portions of streamwise- wall-normal x–y planes coloured by the instantaneous temperature, whose variability clearly reflects Mach number effects (increasing from top to bottom) and diabatic parameter (increasing from left to right). The influence of the Mach number is evident across all cases with an increase in the maximum temperature near the wall, especially in adiabatic cases (right column). However, strong wall cooling (left column) attenuates this effect, as the flow is required to equilibrate with a wall temperature that is considerably lower than the adiabatic wall temperature. These observations are in qualitative agreement with the general trends found in smooth-wall flows at the same M_∞ and Θ (Cogo *et al.* 2023), and are inherently tied to the distribution of wall-normal temperature, reflecting both Mach number (higher T_{aw} with increasing M_∞) and wall cooling effects ($T_w < T_{aw}$ as $\Theta < 1$).

The mean dynamics of the near-wall region is reported as numerical schlieren in figure 3, where we consider both time and spanwise averages. Several important features emerge from this figure. First, the overall darkness of the visualisation varies systematically with wall-thermal conditions: figure 3(*a*) for case M2I appears notably darker than its adiabatic counterpart, figure 3(*b*), and similarly for figures 3(*c*) and 3(*d*) at Mach 4. This reflects the more uniform temperature distribution in isothermal cases noted for figure 2.

https://doi.org/10.1017/jfm.2026.11842 Published online by Cambridge University Press

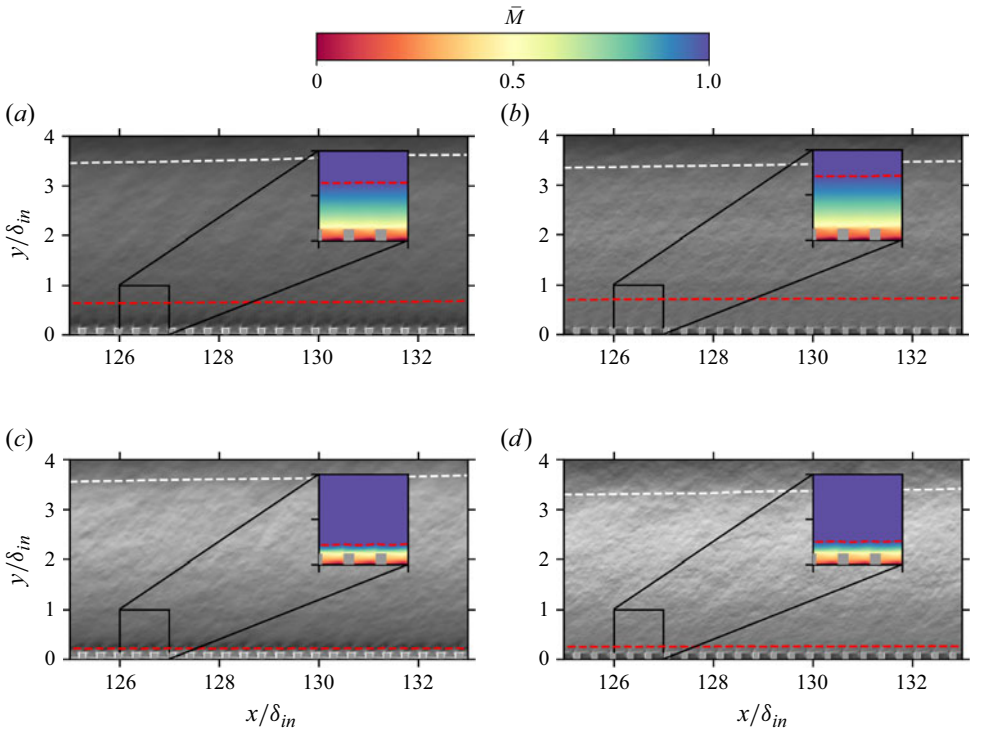


Figure 3. Numerical schlieren $exp(-100|\nabla\bar{\rho}|)$ obtained from the averaged density field $\bar{\rho}/\rho_\infty$ visualised in an x–y slice. Values range from 0.5 to 1.1. In dashed red: sonic line representative of unity local Mach number. White dashed lines represent the boundary-layer thickness δ_{99}. (Inset) Contour of averaged Mach number with values ranging from 0 (red) to 1 (blue). (*a*) M2I, (*b*) M2A, (*c*) M4I, (*d*) M4A.

The red dashed contour line in figure 3 delineates the sonic line, where the local flow velocity magnitude equals the local speed of sound $\bar{a} = \sqrt{\gamma R\bar{T}}$, where R is a specific gas constant, corresponding to unit local Mach number. This contour effectively separates the supersonic outer region from the subsonic near-wall layer. As expected, in the Mach 4 cases the sonic line is located considerably closer to the wall than in Mach 2, indicating that a larger fraction of the BL operates in supersonic conditions. Furthermore, within each Mach number pair, the isothermal-wall cases exhibit sonic lines positioned even closer to the surface. This reflects the reduced near-wall temperature in cooled-wall configurations, which lowers the local speed of sound and causes the sonic condition to be reached at smaller wall-normal distances.

An important observation is that, at the selected measurement station and for both Mach numbers, the roughness elements do not generate discernible shock waves that would introduce large discontinuities in the mean flow. This suggests that the roughness height remains sufficiently submerged within the subsonic layer. This behaviour is also evident in the insets of figure 3, which display the average local Mach number. As reported in table 2, the Mach number at the roughness crest, $\bar{M}_k$, remains below unity, and the ratios between the height of the sonic line and the roughness crest are: 5.35 for M2I, 5.95 for M2A, 1.88 for M4I and 2.08 for M4A. Nevertheless, we do not exclude that at different flow conditions or for more complex roughness configurations, the elements could protrude into the local supersonic region for a portion of their height, potentially generating shock structures, as observed by Peltier, Humble & Bowersox (2016).

https://doi.org/10.1017/jfm.2026.11842 Published online by Cambridge University Press

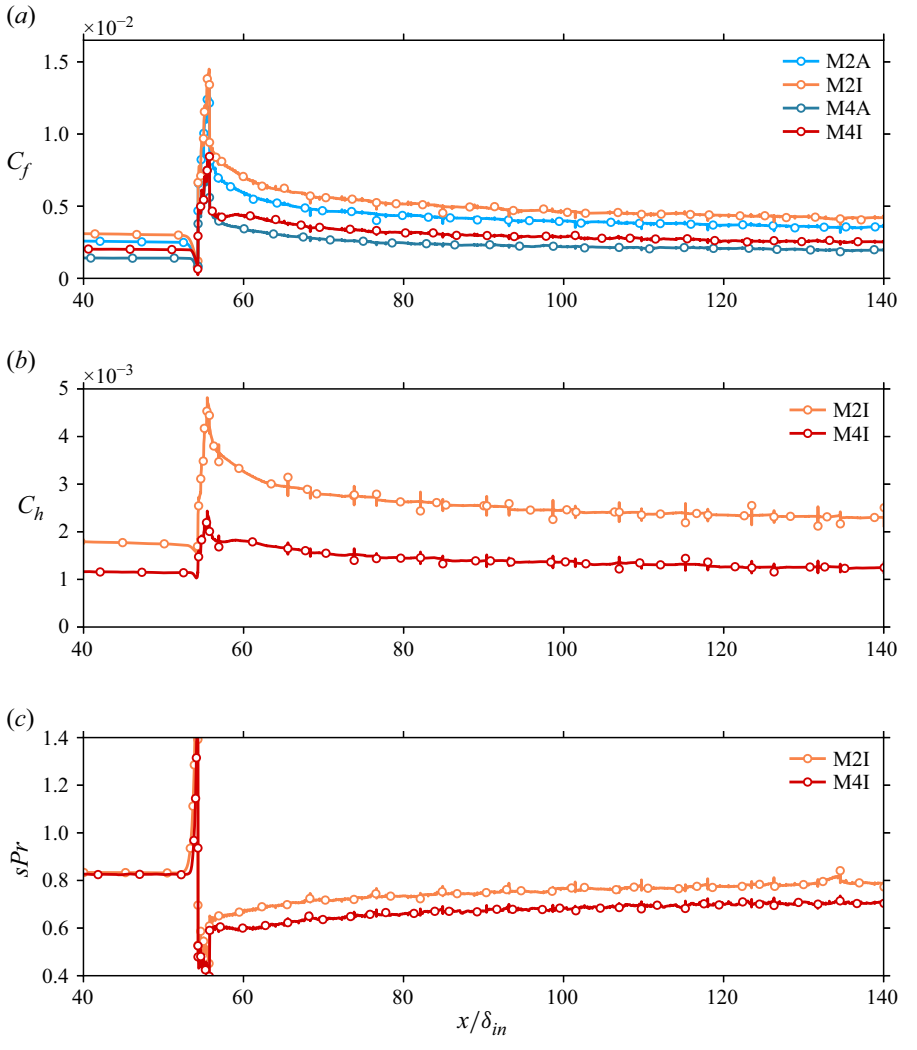


Figure 4. Mean streamwise profiles of (*a*) skin friction coefficient $C_f = \tau_w/(1/2\rho_\infty u_\infty^2)$, (*b*) Stanton number $C_h = q_w/(\rho_\infty u_\infty c_p(T_w - T_r))$, (*c*) RA factor $sPr = 2C_h/C_f Pr$.

Finally, the insets in figure 3, representative of the average local Mach number, show a distinct region of low-momentum fluid in the immediate wake of each roughness element. The spatial extent of this sheltered region, characterised by reduced velocity and elevated temperature relative to the undisturbed flow at the same wall-normal location, plays a crucial role in determining the associated form drag (Cogo *et al.* 2025*b*). This sheltering mechanism has been systematically modelled by Yang *et al.* (2016) for incompressible flows over prism-shaped roughness and will be considered in this study in § 6.

3.2. *Streamwise evolution of wall statistics*

Figure 4 presents the streamwise evolution of key integral quantities following the smooth-to-rough transition at $x/\delta_{in} = 55$; the periodic oscillations visible in the rough-wall region reflect the streamwise-periodic modulation imprinted by the roughness array, spaced at multiples of the roughness wavelength λ.

https://doi.org/10.1017/jfm.2026.11842 Published online by Cambridge University Press

Figure 4(*a*) shows the skin friction coefficient C_f for all four configurations. A sharp peak occurs immediately downstream of the transition, followed by a gradual relaxation as the flow adjusts to the new wall condition, consistent with previous studies (Rouhi, Chung & Hutchins 2019; Cogo *et al.* 2025*b*). The influence of Mach number and wall temperature in the rough region follows the same trends as the smooth-wall counterpart (Huang, Duan & Choudhari 2022; Cogo *et al.* 2023): C_f decreases with increasing Mach number and increases with wall cooling ($T_w < T_{aw}$).

Figure 4(*b*) shows the Stanton number C_h for the isothermal cases (M2I, M4I), which exhibits qualitatively similar behaviour to C_f. The case M2I consistently shows higher heat transfer than M4I in both smooth and rough regions. Both cases show a gradual decay downstream of the transition, with M2I maintaining approximately twice the heat transfer rate of M4I throughout the domain.

Figure 4(*c*) presents the RA factor multiplied by the Prandtl number, sPr, where $s = 2C_h/C_f$. This is a classical integral measure of the RA that has been extensively studied in smooth-wall flows (Zhang *et al.* 2014; Wenzel *et al.* 2022; Cogo *et al.* 2023). These studies showed that smooth-wall compressible flows exhibit excellent universality, with $sPr = 0.8 \pm 0.03$ (Cogo *et al.* 2023) regardless of Mach number, wall temperature or Reynolds number. This value is clearly observed here for both M2I and M4I in the smooth region before the onset of roughness. After the smooth-to-rough transition, both cases show a dramatic drop to $sPr \approx 0.4$–0.5 at the transition, followed by gradual relaxation that does not recover the smooth-wall reference value. More importantly, M4I exhibits a distinctly lower sPr than M2I, undermining its universality among rough-wall cases.

This behaviour is well documented not only in high-speed flows but also in incompressible wall-bounded flows with heat transfer (Bons 2005), where sPr varies significantly depending on the roughness geometry. This fact reflects the fundamental differences between momentum transport (dominated by form drag on roughness elements) and heat transfer (governed by thermal conduction) in the roughness sublayer, which prevent the use of an integral indicator for the RA (Owen & Thomson 1963). Despite this, § 4 demonstrates that a local formulation of the RA for the mean flow can still be applied outside the direct influence of roughness. We address this by examining a wall-normal location far from the roughness transition, at $x/\delta_{in} = 127$, where all cases appear reasonably equilibrated.

4. Validity of the Reynolds analogy

4.1. *Framework of the Reynolds analogy for mean flows*

The formulation of the RA for mean flows, generalised by Zhang *et al.* (2014), establishes a direct relation between the mean velocity $\bar{u}$ and the defect of a generalised recovery enthalpy, $\bar{H}_g - \bar{H}_w$, namely

$$\bar{H}_g - \bar{H}_w = U_w \bar{u}, \tag{4.1}$$

where $H_g = c_p T + r_g u^2/2$ is a generalised recovery enthalpy defined in terms of the recovery factor r_g.

Equation (4.1) implies that the proportionality between the mean enthalpy and velocity fields is governed by a constant velocity scale U_w. Rewriting (4.1) in terms of temperature yields a quadratic relation between the mean temperature and velocity

$$\bar{T} = T_w + \frac{U_w}{c_p}\bar{u} - \frac{r_g}{2c_p}\bar{u}^2, \tag{4.2}$$

https://doi.org/10.1017/jfm.2026.11842 Published online by Cambridge University Press

which satisfies the wall boundary condition $\bar{T} = T_w$ when $\bar{u} = 0$. In this formulation, the coefficients U_w and r_g determine the linear and quadratic contributions of the velocity field to the temperature distribution.

Equation (4.2) provides a convenient framework to interpret several classical temperature–velocity relations proposed in the literature, which can be viewed as particular closures for the coefficients U_w and r_g depending on the assumed coupling between momentum and heat transfer.

4.2. *Classical formulations*

The earliest form of this relation can be traced back to the Crocco–Busemann theory (Crocco 1932), derived for compressible BLs under the assumptions of constant properties and unit Prandtl number. Under these conditions the quadratic coefficient reduces to $r_g = 1$, while the linear coefficient depends on the difference between wall and stagnation temperatures, leading to a temperature–velocity relation based on the stagnation temperature T_0.

For turbulent BLs, Walz (1969) introduced the concept of recovery temperature T_r to account for the departure from unity of the Prandtl number. This modification introduces a recovery factor r, typically approximated as $r \approx Pr^{1/3}$, which replaces the unit coefficient of the Crocco formulation and yields the well-known Walz relation.

Alternative formulations express the temperature–velocity relation directly in terms of wall fluxes. In particular, the model proposed by Huang & Coleman (1994) relates the linear coefficient to the ratio between wall heat flux and wall-shear stress, q_w/τ_w, together with an effective Prandtl number Pr_e representing a combination of molecular and turbulent transport effects, whose best fit from DNSs has been reported as $Pr_e \approx 0.8$ (Larsson & Pirozzoli 2026). This approach is convenient when wall fluxes are known or can be estimated.

More recently, Zhang *et al.* (2014) proposed a generalised recovery factor r_g that depends explicitly on both the wall heat flux and the external flow conditions. In this formulation, the coefficients of (4.2) are obtained by simultaneously enforcing the outer boundary condition and the relation between wall heat and momentum fluxes, providing a unified framework that recovers the Crocco and Walz analogies as limiting cases for $Pr = 1$ and adiabatic conditions.

The formulations described above can be systematically characterised by the degree of freedom they assign to the coefficients of (4.2). The Crocco–Busemann and Walz relations prescribe both r_g and the functional form of U_w, leaving no free parameters once the outer boundary condition is imposed. The Huang & Coleman (1994) relation similarly fixes $r_g = Pr_e$, expressing U_w through the wall-flux ratio q_w/τ_w. In contrast, the GRA of Zhang *et al.* (2014) leaves r_g as a free parameter, determining it self-consistently by simultaneously enforcing the outer boundary condition and the wall-flux relation. A summary of these formulations and their corresponding coefficients is reported in table 3.

4.3. *Wall-modelling closures*

The RA factor s represents an integral measure of the momentum–energy coupling across the entire BL (Wenzel *et al.* 2022). Its departure from universality in rough-wall flows therefore does not imply that the local analogy between the mean momentum and energy equations breaks down everywhere in the flow. This observation motivates a local assessment of the temperature–velocity relation outside the roughness sublayer, which is

https://doi.org/10.1017/jfm.2026.11842 Published online by Cambridge University Press

Approach	Equation	Total temperature	Recovery factor
General	$\bar{T} = T_w + c_1\bar{u} - c_2\bar{u}^2$	—	—
Crocco (1932)	$\bar{T} = T_w + \dfrac{T_0 - T_w}{u_\delta}\bar{u} - \dfrac{1}{2c_p}\bar{u}^2$	$T_0 = T_\delta + \dfrac{u_\delta^2}{2c_p}$	—
Walz (1969)	$\bar{T} = T_w + \dfrac{T_r - T_w}{u_\delta}\bar{u} - \dfrac{r}{2c_p}\bar{u}^2$	$T_r = T_\delta + r\dfrac{u_\delta^2}{2c_p}$	$r = Pr^{1/3}$
Huang & Coleman (1994)	$\bar{T} = T_w - \dfrac{Pr_e\, q_w}{c_p\tau_w}\bar{u} - \dfrac{Pr_e}{2c_p}\bar{u}^2$	—	$Pr_e \approx 0.8$
Zhang *et al.* (2014)	$\bar{T} = T_w + \dfrac{T_{r_g} - T_w}{u_\delta}\bar{u} - \dfrac{r_g}{2c_p}\bar{u}^2$	$T_{r_g} = T_\delta + r_g\dfrac{u_\delta^2}{2c_p}$	$r_g = \dfrac{T_w - T_\delta}{u_\delta^2/(2c_p)} - 2\dfrac{Prq_w}{\tau_w u_\delta}$

Table 3. Original formulation of the RA for the mean temperature–velocity relation with various approaches. In smooth-wall flows, the formulations that rely on the unknown ratio q_w/τ_w can be closed by invoking the universality of the RA factor $s\,Pr = 2C_h/C_f\,Pr \approx 0.8$.

the focus of § 4.4. Before doing so, we reformulate the classical closures in a form suitable for wall-modelling applications.

When (4.2) is employed for wall-modelling purposes, the classical formulations face two difficulties that must be addressed before they can be applied to rough-wall flows.

In smooth-wall flows, the universality of the RA factor $s \approx 0.8/Pr$ provides a direct route from wall-shear stress to heat flux. As shown in figure 4, this universality breaks down over rough surfaces, where s varies significantly with roughness geometry and flow conditions. The wall-flux ratio q_w/τ_w therefore cannot be prescribed *a priori*. Instead, our objective is to infer q_w indirectly by exploiting the temperature–velocity relation (4.2). If U_w can be determined by other means, the inner-layer consistency condition obtained by differentiating (4.2) at the wall

$$U_w^{in} = -Pr\frac{q_w}{\tau_w}, \tag{4.3}$$

provides an estimate of q_w once τ_w is known from a momentum wall model.

In classical formulations, U_w is determined by enforcing the outer boundary condition at the boundary-layer edge $y = \delta$. In complex configurations, and in particular for wall-modelling purposes, the boundary-layer edge may not be robustly identifiable. A more practical approach is to determine U_w by evaluating (4.2) far from the roughness layer at an intermediate matching location $y = y_m$ within the logarithmic (overlap) region, where both velocity and temperature are available. This yields

$$U_w^m = c_p\frac{T_{r,y}\big|_{y=y_m} - T_w}{u|_{y=y_m}}, \tag{4.4}$$

where $T_{r,y} = T + r_g u(y)^2/(2c_p)$ denotes the local recovery temperature. The resulting formulations, expressed using U_w^m in place of edge quantities, are summarised in table 4.

For the Walz-like approach, the recovery factor is prescribed as $r_g = Pr^{1/3}$, so U_w^m is the only quantity to be determined and a single matching location y_m suffices to fully specify the temperature–velocity relation. The wall heat flux is then obtained through the consistency condition $U_w^m = U_w^{in}$, which gives $q_w = -\tau_w U_w^m/Pr$.

https://doi.org/10.1017/jfm.2026.11842 Published online by Cambridge University Press

Approach	T-u relation	Total temperature	Recovery factor
Walz (1969)	$\bar{T} = T_w + \frac{U_w^m}{c_p}\bar{u} - \frac{r}{2c_p}\bar{u}^2$	$T_r = T_m + r\frac{u_m^2}{2c_p}$	$r = Pr^{1/3}$
Huang & Coleman (1994)	$\bar{T} = T_w + \frac{U_w^m}{c_p}\bar{u} - \frac{Pr_e}{2c_p}\bar{u}^2$	$T_r = T_m + Pr_e\frac{u_m^2}{2c_p}$	$Pr_e \approx 0.8$
Zhang *et al.* (2014)	$\bar{T} = T_w + \frac{U_w^m}{c_p}\bar{u} - \frac{r_g}{2c_p}\bar{u}^2$	$T_{r_g} = T_m + r_g\frac{u_m^2}{2c_p}$	$r_g = \frac{T_w - T_\delta}{u_\delta^2/(2c_p)} + 2\frac{U_w^m}{u_\delta}$

Table 4. Modified formulation of the RA for the mean temperature–velocity relation with various approaches considering wall model applications. The value of U_w^m is computed using knowledge of the matching location, (4.4). The modified approach of Zhang *et al.* (2014) is equivalent to the general approach of table 3, with c_1 and c_2 computed from matching and edge locations.

The closure of Huang & Coleman (1994) similarly prescribes the quadratic coefficient as $r_g = Pr_e \approx 0.8$, so again a single matching location fully determines the relation. In this case, the inner estimate becomes $U_w^m = -Pr_e q_w/\tau_w$, providing q_w directly once τ_w is available. We note that this relation is not formally consistent with the exact wall derivative given by (4.3), since $Pr_e \neq Pr$. Rather, Pr_e acts as an empirical correction that absorbs both molecular and turbulent transport effects, and has been shown to yield accurate predictions in smooth-wall DNSs (Larsson & Pirozzoli 2026).

The GRA proposed by Zhang *et al.* (2014) is less convenient in this context, because r_g is not prescribed *a priori* but is instead determined self-consistently by combining the outer boundary condition with the wall-flux relation. In practice, this requires information at two locations simultaneously: one within the logarithmic region (to determine U_w) and one at the boundary-layer edge (to determine r_g). As a consequence, the GRA cannot be reformulated using a single matching location alone and retains a dependence on edge quantities. This makes it less attractive for general wall-modelling applications, although it remains applicable when free-stream values can be estimated.

The framework described above rests on a key assumption: that the presence of roughness modifies the effective boundary condition of the temperature–velocity relation without altering its functional form outside the roughness sublayer. Under this hypothesis, consistent with the outer-layer similarity arguments of Townsend (1980), the parabolic relation (4.2) remains sufficiently valid above the roughness crest, and the coefficients U_w and r_g can be determined from information at the matching location y_m without any explicit modelling of the roughness-sublayer physics. The validity of this assumption is assessed in § 4.4.

4.4. *Validation of RA for the present dataset*

We now assess the validity of the aforementioned models against the present rough-wall DNS database, which includes both adiabatic and diabatic cases over a range of Mach numbers. Each model is evaluated from two complementary perspectives. First, we determine how accurately the predicted temperature–velocity relation reproduces the DNS profiles when the parabolic coefficients U_w and r_g are computed exclusively from outer-layer information (i.e. $U_w = U_w^m$). Second, we examine the consistency with near-wall behaviour by comparing U_w^m with its inner counterpart, U_w^{in}.

https://doi.org/10.1017/jfm.2026.11842 Published online by Cambridge University Press

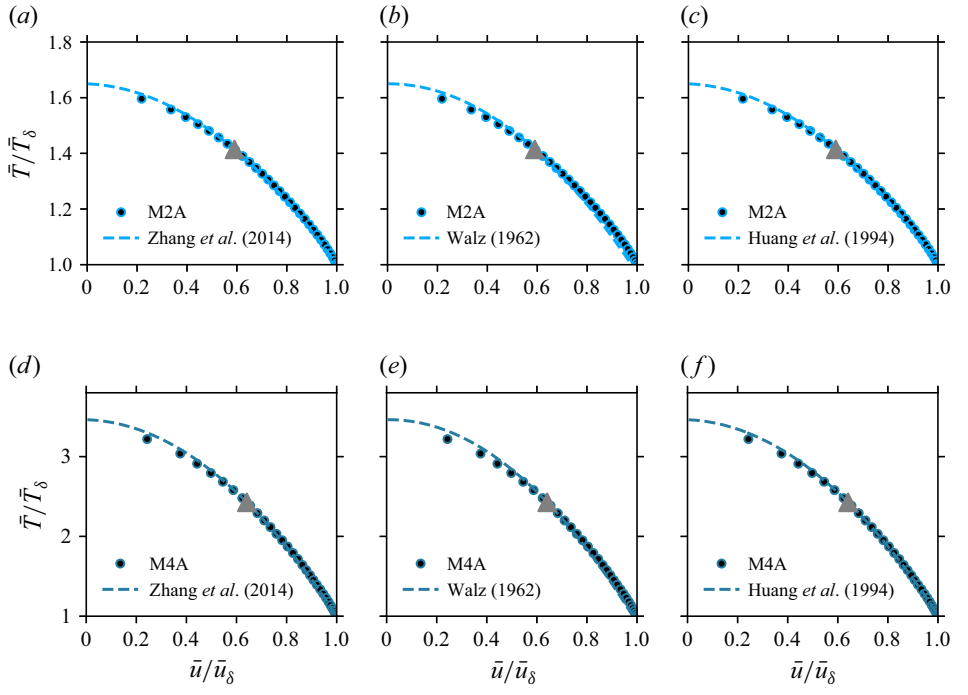


Figure 5. Comparison of the three temperature–velocity closures (Walz 1969; Huang & Coleman 1994; Zhang *et al.* 2014; left to right) against the DNS rough-wall database at selected station $x = 127\delta_{in}$. Top row: M2A; bottom row: M4A. The solid curves represent the model predictions obtained using outer-layer information only, evaluating DNS data at $y^+ = 300$ (which location is highlighted by the grey triangle). Dots indicate the DNS temperature–velocity relation, excluding the roughness sublayer.

To address these points, DNS velocity and temperature profiles are sampled at a representative location in the logarithmic (overlap) layer, $y^+ = 300$. This procedure provides a consistent estimate of U_w^m for each model, following the methodology summarised in table 4. We underline that the approach of Zhang *et al.* (2014) requires also the knowledge of BL values at δ, as discussed previously, and suffers from an indeterminate form if the matching location approaches the boundary-layer edge δ.

Figures 5 and 6 illustrate the results for each model for both adiabatic and isothermal cases, respectively. For the latter, we assess both the adequacy of the outer-layer parabolic fit (common to both figures) and the resulting prediction of the wall gradient, $\partial T/\partial u|_w = U_w/c_p$, using either U_w^{in} or U_w^m to compute U_w.

With respect to the global parabolic behaviour, all three closures capture the overall quadratic structure of the $T(u)$ relation at both Mach numbers and wall temperature conditions. For isothermal cases, figure 6, the Walz (1969) and Zhang *et al.* (2014) formulations provide the closest agreement with the DNS curvature, while the Huang & Coleman (1994) relation exhibits a slight underprediction in the vicinity of the temperature maximum. Overall, all approaches show a good agreement of the parabolic fit for velocities greater than $0.4\bar{u}/\bar{u}_\delta$, which corresponds to $y^+ \gtrsim 150$. This suggests that the direct influence of roughness elements fades out at approximately 2–3 times the roughness height (in the present database $k^+ \approx 60$). This value is in agreement with the expected end of the roughness sublayer, which has been reported to be between two and five times the roughness height (Jiménez 2004; Williams *et al.* 2021).

https://doi.org/10.1017/jfm.2026.11842 Published online by Cambridge University Press

Case	ϵ_{q_w} [%] ($M_\infty = 2$)	ϵ_{q_w} [%] ($M_\infty = 4$)
Walz (1969)	27.59	38.78
Huang & Coleman (1994)	5.61	14.02
Zhang *et al.* (2014)	25.93	35.81

Table 5. Relative error in the prediction of q_w for cases M2I and M4I, using the correct τ_w from DNSs at different Mach numbers.

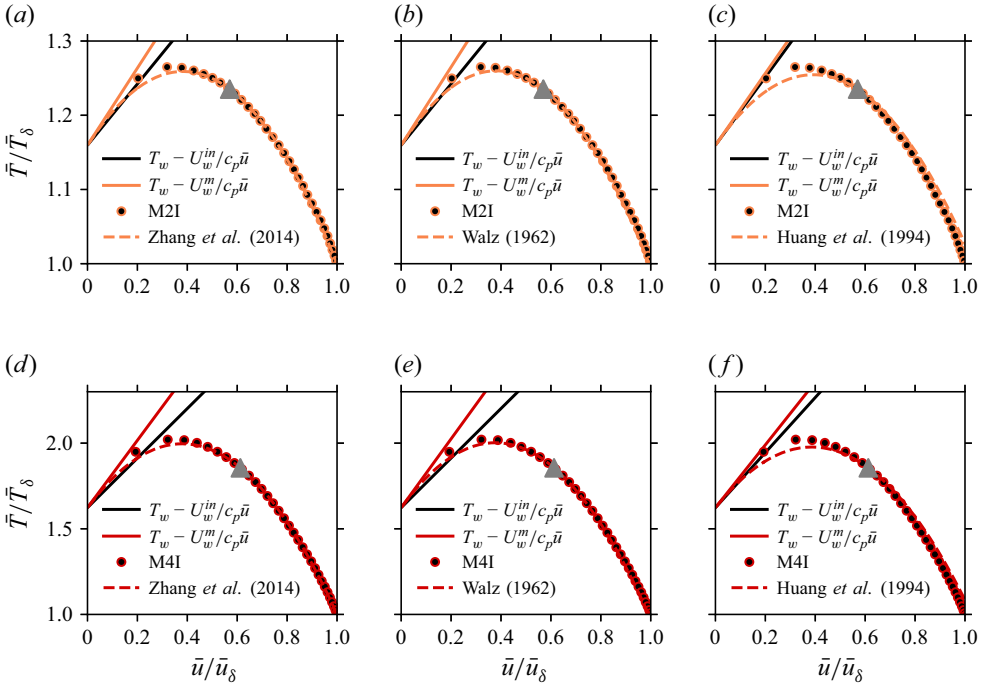


Figure 6. Comparison of the three temperature–velocity closures (Walz 1969; Huang & Coleman 1994; Zhang *et al.* 2014; left to right) against the DNS rough-wall database at selected station $x = 127\delta_{in}$. Top row: M2I; bottom row: M4I. The solid curves represent the model predictions obtained using outer-layer information only, evaluating DNS data at $y^+ = 300$. Dots indicate the DNS temperature–velocity relation, excluding the roughness sublayer. The straight lines near the wall show the predicted wall gradient, $\partial T/\partial u|_w = U_w/c_p$, using either the outer-layer estimate U_w^m (orange for M2I and red for M4I) or the inner-layer estimate U_w^{in} (black).

A different ranking emerges when examining the wall gradients $\partial T/\partial u|_w$, shown only for isothermal cases in figure 6. The comparison between the inner-based and outer-based estimates (U_w^{in} versus U_w^m) shows that the Huang & Coleman (1994) formulation yields the smallest separation between the corresponding straight-line slopes at both Mach numbers. On the other hand, Walz (1969) and Zhang *et al.* (2014) appear to have similar discrepancies. A quantitative assessment of the error incurred when evaluating q_w by relating the definitions of the coefficients of the linear term for each T–u relation of tables 3 and 4, which is important for wall-modelling implications of § 6, is reported in table 5. This confirms the trends obtained by visual inspection of figure 6, while clarifying the approach of Zhang *et al.* (2014) yields marginally better predictions than Walz (1969).

https://doi.org/10.1017/jfm.2026.11842 Published online by Cambridge University Press

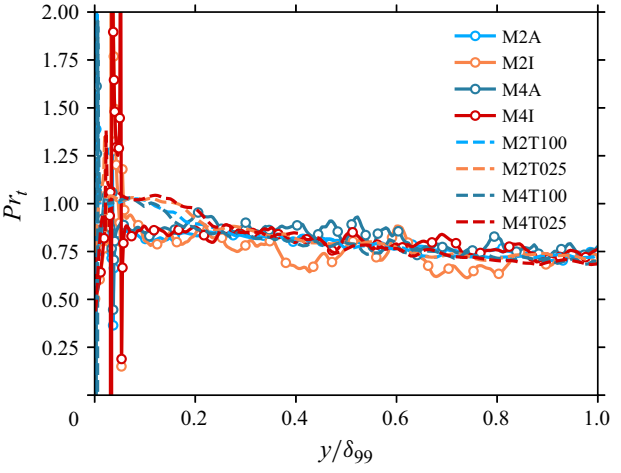


Figure 7. Turbulent Prandtl number Pr_t as a function of y/δ_{99} for the present rough-wall database. Smooth-wall references (dashed lines) are taken from Cogo *et al.* (2023) at $Re_\tau = 443$, and are reported in the legend using the same labels as the original paper.

These results demonstrate that an accurate reproduction of the outer-layer $T(u)$ relation does not, by itself, ensure consistency in the near-wall limit. In other words, capturing the correct global parabolic behaviour is not sufficient to guarantee an accurate wall gradient. This highlights the need for a modelling strategy that reconciles near-wall and parabolic fit accuracies rather than privileging one at the expense of the other. In this respect, the relatively good performance of the formulation by Huang & Coleman (1994) may not be coincidental: its underlying assumption of a mixed Prandtl number, blending molecular and turbulent contributions, naturally embeds information from both the inner and outer turbulent regions.

Figure 7 shows the turbulent Prandtl number Pr_t as a function of wall-normal distance y/δ_{99} for all cases considered. In the region very close to the wall ($y/\delta_{99} \lesssim 0.05$), all rough-wall cases (solid lines) exhibit a sharp spike in Pr_t. This spike is confined to the roughness sublayer, where the direct influence of the roughness elements disrupts the typical momentum and thermal transport mechanisms. Beyond this narrow region ($y/\delta_{99} \gtrsim 0.1$), the turbulent Prandtl number quickly relaxes to values around $Pr_t \approx 0.9$ and remains in accordance with smooth-wall references of Cogo *et al.* (2023) throughout the outer layer.

This preservation of the smooth-wall turbulent Prandtl number in the outer layer provides physical support for the applicability of the Huang & Coleman (1994) approach to rough-wall flows. Since their formulation was originally developed for smooth walls, the fact that $Pr_t \approx 0.9$ remains unchanged outside the roughness sublayer suggests that the underlying assumptions about turbulent transport remain valid. This explains why their mixed Prandtl number $Pr_e \approx 0.8$ continues to provide accurate predictions of the temperature–velocity relation and wall heat flux, even in the presence of roughness, without the need of additional tuning.

In general, these preliminary results indicate that the local parabolic formulation of the RA appears to remain a viable and structurally consistent modelling assumption, and roughness effects are transmitted to the outer layer only indirectly, through a modification of the effective boundary conditions, in accordance with the Townsend (1980) outer-layer similarity hypothesis.

https://doi.org/10.1017/jfm.2026.11842 Published online by Cambridge University Press

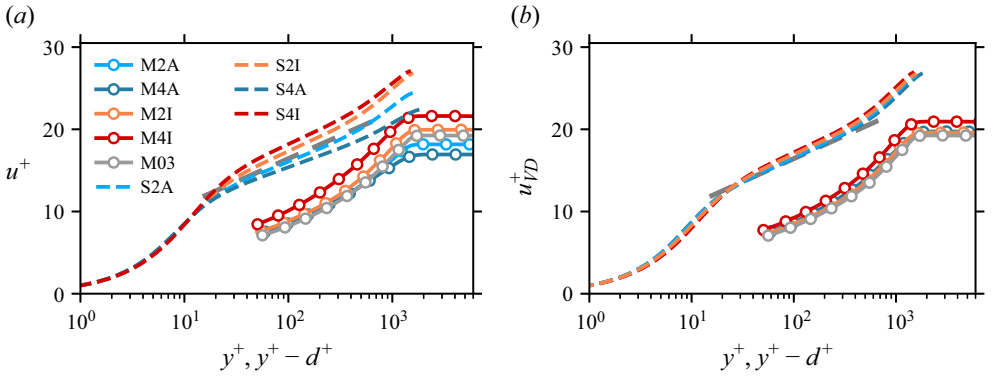


Figure 8. Comparison between the mean velocity profile u^+ as function of y^+ before (*a*) and after (*b*) applying the transformation of Van Driest (1951). Rough-wall cases are shifted in the wall-normal direction by the virtual origin d. Grey lines represent the log law $u^+ = (1/\kappa)\, ln(y^+) + 5.2$. The subsonic case M03 from Cogo *et al.* (2025*a*), which has the same roughness pattern, is included for reference.

5. Outer-layer similarity for the velocity field

For compressible velocity fields, the classical approach to obtaining the outer-layer similarity is the use of compressible transformations, that aim to account for variations of mean flow properties in order to recover the incompressible profiles, for which outer-layer similarity over certain roughness patterns is much more established (Cogo *et al.* 2025*a*).

In this study, we consider the classical Van Driest (1951) transformation, here denoted by the subscript 'VD', which accounts for mean-density variations in order to yield an incompressible-like velocity profile u_{VD}, such that $u_{VD} = \int_0^u \sqrt{\bar{\rho}/\bar{\rho}_w}\, \mathrm{d}u$. This particular transformation has been selected given its simple formulation, which can be easily incorporated in rough-wall models, and given the fact that only the log layer region is of interest, where a density-based scaling is physically consistent.

Figure 8 reports both smooth-wall profiles (S2A, S2I, S4A, S4I), and rough-wall ones (M2A, M2I, M4A, M4I), in both classical inner units, panel (*a*), and by using Van Driest (1951) transformation, panel (*b*). Here, the wall-normal coordinate used for rough-wall profiles is shifted by the same virtual origin $d = k$ (Chung *et al.* 2021), consistent with the previous work of Cogo *et al.* (2025*b*).

When observed in classical inner units, panel (*a*), both smooth- and rough-wall profiles are sensitive of the compressibility effects and wall temperature conditions, especially in the log layer. Here, while smooth-wall profiles have a well-established incompressible reference, the log law, rough-wall counterparts are compared with the nearly incompressible case provided by Cogo *et al.* (2025*a*), which shares the same roughness pattern and similar flow conditions. When the Van Driest (1951) transformation is applied to all cases, we observe a good collapse of both smooth and rough profiles with their respective incompressible reference, with only a minor mismatch for the case M4I, a sign that for our set-up compressibility effects are still well captured by velocity transformations. This observation is another important building block for wall-modelling efforts, providing a way to leverage the much more extensive theoretical framework existing for incompressible flows by using compressibility transformations.

We note that several recent compressibility transformations have been proposed that supersede the classical work of Van Driest (1951), such as Trettel & Larsson (2016), Griffin, Fu & Moin (2021) and Hasan *et al.* (2023). However, these formulations have been developed and validated exclusively for smooth-wall flows (Huang *et al.* 2022;

https://doi.org/10.1017/jfm.2026.11842 Published online by Cambridge University Press

Zhang, Duan & Choudhari 2018; Cogo *et al.* 2023). This is a crucial distinction, since the only region of similarity that can be exploited between smooth and rough flows is the log layer, while the viscous and buffer layers are typically disrupted by the presence of roughness. Additionally, more recent transformations still incorporate the density-based scaling proposed by Van Driest (1951) in the log layer, while mainly adding refined physical arguments for the viscous sublayer. We have nevertheless tested these more recent transformations and found that they do not show better performance than Van Driest (1951) for the present rough-wall cases (not shown). Future rough-wall compressibility transformations should therefore build upon a density-based scaling for the logarithmic layer while accounting for the inherently different near-wall dynamics imposed by rough walls.

6. Formulation of a wall model

In this section, we propose a physics-based wall model for compressible flows over distributed prism-shaped roughness. The objective is to predict the wall-shear stress τ_w and wall heat flux q_w from mean flow properties at the matching location, roughness geometry and wall temperature. The model is constructed around three building blocks: (i) a drag-predictive rough-wall model that estimates τ_w, (ii) a compressibility correction that extends it to high-speed flows and (iii) a RA-based closure that enables temperature–velocity coupling, as well as estimation of the wall heat flux q_w.

To estimate the roughness-induced wall-shear stress τ_w, we adopt the physics-based roughness model of Yang *et al.* (2016), originally developed for incompressible flows over prism-shaped roughness. In this section, we only highlight the main equations of this method, including the proposed extension to account for high-speed flows, while the reader can find the specific closure of each parameter in Appendix A and in the original paper.

In the framework introduced by Yang *et al.* (2016), the mean velocity profile above the rough surface can be obtained by combining a logarithmic region valid above the roughness crest with an exponential attenuation layer within the roughness canopy. In the roughness sublayer ($y < k$), the mean velocity is assumed to follow

$$\bar{u}(y) = \bar{u}_k \exp\left[a\frac{(y-k)}{k}\right], \tag{6.1}$$

where $\bar{u}_k$ is the velocity at the roughness crest, a is an attenuation factor accounting for sheltering effects between elements and k is the roughness height. The parameters a and the associated virtual origin d are determined from both flow conditions and geometrical considerations (see Appendix A). We note that the functional form of (6.1), motivated by the physical modelling of Reynolds-averaged streamwise momentum equation (Yang *et al.* 2016), does not satisfy the correct zero velocity condition at the wall $y = 0$, whose compliance would have severely undermined its simplicity. Nevertheless, it has been shown to approximate very well the velocity at the roughness crest, which then provides a matching condition for the logarithmic law. For this reason, and considering that all flows in the present database are subsonic below the roughness crest (see figure 3), we choose not to consider compressibility corrections for this equation.

Above the crest ($y > k$), the mean velocity satisfies the logarithmic law, in accordance to the outer-layer similarity Chung *et al.* (2021) typical of the fully rough regime (Jiménez 2004). In compressible flow, this is written in differential form aspage

https://doi.org/10.1017/jfm.2026.11842 Published online by Cambridge University Press

$$\frac{\mathrm{d}\bar{u}}{\mathrm{d}y} = \frac{u_\tau}{\kappa}\frac{1}{y-d}\sqrt{\frac{\bar{\rho}_w}{\bar{\rho}}}, \tag{6.2}$$

where κ is the von Kármán constant and d is the virtual origin.

The appearance of the density ratio comes from the velocity transformation of Van Driest (1951), which maps the compressible mean velocity to an equivalent incompressible form by incorporating mean-density variations. This ratio is evaluated using the ideal-gas relation under the zero-pressure-gradient assumption ($p \approx p_\delta$) and the temperature profile obtained from the RA-based closure $T(u)$.

The differential form of the logarithmic law, (6.2), efficiently incorporates the compressibility correction of Van Driest (1951), however, it prevents a direct coupling with the exponential layer defined by (6.1), which in the original formulation was enforced by matching the velocity profile at $y = k$.

In order to compel a match between the two layers through the velocity $\bar{u}_k$, as well as providing the lower integration bound for (6.2), we consider the analytical solution of the same equation only for the roughness crest $y = k$

$$\bar{u}_k = \frac{u_\tau}{\kappa}\ln\left(\frac{k-d}{z_0}\right), \tag{6.3}$$

where z_0 is the hydrodynamic roughness length, determined by the roughness geometry and flow conditions (see Appendix A). The rationale for this approach is that mean-density variations mainly alter the compressible velocity profiles in the outer layer, while from the wall up to the roughness crest they are relatively small and force a minor departure from the incompressible logarithmic law (see figure 8). We note that this assumption applies only to the momentum–energy coupling in a specific region of the flow. Thermodynamic quantities, including temperature and density, are still allowed to vary throughout the whole BL and are reconstructed through the temperature–velocity relation during the outer-layer matching procedure, such that $T|_{y=k} \neq T_w$ (thus $\rho|_{y=k} \neq \rho_w$).

By combining (6.1) and (6.3) we can obtain an expression for both z_0, a and d, as well as the ratio $\bar{u}_k/u_\tau$. However, the value of u_τ is known only after integrating (6.2) from $y = k$ to the matching location $y = y_m$, thus is affected by compressibility effects prescribed by the density ratio. Once u_τ is determined, the wall-shear stress follows as $\tau_w = \bar{\rho}_w u_\tau^2$.

Having established the momentum closure, we introduce the thermal model, which is coupled to the former through density. The validation study in § 4 showed that accurately reproducing the outer-layer parabolic $T(u)$ relation does not automatically guarantee correct near-wall behaviour. Among the closures examined, the formulation of Huang & Coleman (1994) provided the best compromise between outer-layer accuracy and wall-gradient consistency. Although the present approach remains consistent with all formulations, we adopt the Huang & Coleman (1994) temperature–velocity relation as the thermal closure

$$\bar{T} = T_w + \frac{U_w^m}{c_p}\bar{u} - \frac{Pr_e}{2c_p}\bar{u}^2, \tag{6.4}$$

where $Pr_e = 0.8$ and U_w^m is determined from outer-layer information using the matching procedure as reported in (4.4). Through this relation, temperature, density and velocity become fully coupled during the integration of the mean velocity profile.

Finally, once τ_w is known, the wall heat flux q_w is obtained consistently from the equivalence of U_w^m and U_w^{in} for the approach of Huang & Coleman (1994)

https://doi.org/10.1017/jfm.2026.11842 Published online by Cambridge University Press

$$q_w = -\tau_w \frac{U_w^m}{Pr_e}. \tag{6.5}$$

Using the present approach, the wall heat flux is indirectly inferred from its impact on the flow variables at the matching location, avoiding the need to explicitly resolve roughness-induced forcing terms in the averaged energy equation.

Before analysing the performance of the present wall model, we note that one of its main strengths lies in its modular formulation. The model is constructed from individual building blocks that can be independently assessed and systematically improved in future developments, rather than relying entirely on semi-empirical tuning parameters. This structure enables the straightforward incorporation of additional physical ingredients, such as velocity models suitable for more complex roughness patterns, compressibility transformations that better capture high-speed effects, or alternative formulations based on RA.

Additionally, semi-empirical correlations that have been proposed in the past to account for the non-universality of the RA factor $s = 2C_h/C_f$ in rough-wall flows can be readily incorporated into the present framework. An example is the correlation proposed by Hill *et al.* (1980), developed for rough slender cones at hypersonic speeds. In the present notation, this correlation can be written as

$$C_h = C_f \frac{s_{smooth}}{2} \left[1 + \beta \sqrt{\frac{T_w}{T_\delta} \frac{C_f}{2}} k^{+0.45} \, \mathrm{Pr}^{0.8} \right]^{-1}, \tag{6.6}$$

where β typically ranges from 0.4 to 1.3 depending on the specific configuration (Bowersox 2007), and $s_{smooth} = C_{h,s}/C_{f,s}$ denotes the RA factor of the corresponding smooth-wall reference case, which can be taken with the corresponding value $s_{smooth} Pr = 0.8 \pm 0.03$ (Cogo *et al.* 2023).

It is worth noting that both C_f and k^+ appear as unknown quantities in the correlation of Hill *et al.* (1980), whereas they are directly available within the present wall-model formulation which accounts for compressibility effects. Consequently, (6.6) can, in principle, be used in place of (6.5) in order to estimate the wall heat flux q_w, provided that prior evidence supports the suitability of this approach for the specific application under consideration.

7. *A priori* results

In this section, the proposed model is tested *a priori* using the DNSs of the present dataset, listed in table 2. In particular, the mean DNS flow field is sampled at the matching location, and related flow variables are fed to the model, which in response provides an estimate of mean velocity and temperature profiles, as well as wall fluxes τ_w and q_w.

Following the analysis of § 4, the lower bound for choosing the matching location should be approximately $y^+ \approx 150$, which agrees with the end of the roughness sublayer and above which all parabolic fits start to show good agreement with DNS data. Additionally, wall-modelling applications generally target a matching region within the logarithmic (overlap) layer, which generally corresponds to 0.1–0.2 Re_τ. With these constraints, and considering the friction Reynolds numbers found in the present database, we sample our DNS database at $y_m^+ = 150$ and $y_m^+ = 300$ in order to assess different matching locations in the intended range of applicability of the model.

Figure 9 shows the model's prediction of the mean velocity and temperature profiles of the adiabatic and isothermal BLs over aligned cubical elements for the most challenging matching location ($y_m^+ = 300$). Panels (*a–b*) show cases at $M_\infty = 2$, M2A and M2I, while

https://doi.org/10.1017/jfm.2026.11842 Published online by Cambridge University Press

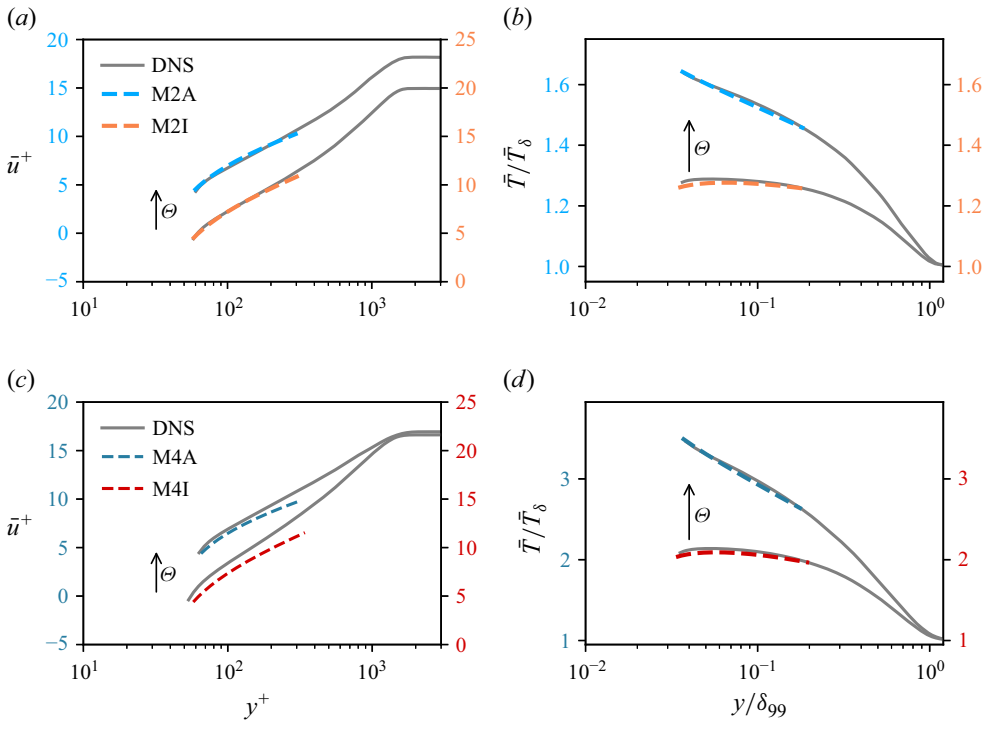


Figure 9. Mean rescaled velocity (*a*,*c*) and temperature (*b*,*d*) profiles as function of the wall-normal coordinates y^+ and y/δ_{99}, respectively. Panels (*a*,*b*) report cases at $M_\infty = 2$, and panels (*c*,*d*) at $M_\infty = 4$. Each figure shows two wall temperature conditions: adiabatic ($\Theta \approx 1$) and cold wall ($\Theta = 0.25$). For the velocity profiles, adiabatic cases (M2A and M4A) are manually shifted upwards by $\Delta u^+ = 5$ (left axis) in order to distinguish them from cold wall cases (right axis). The matching location for the model is located at $y_m^+ = 300$.

panels (*c*–*d*) show cases at $M_\infty = 4$, M4A and M4I. Here, the model outputs are shown from the roughness crest $y = k$, up to the matching location $y = y_m$. In general, there is an excellent agreement between the model outputs and the reference DNS profiles, with minor deviations only for the velocity profiles at $M_\infty = 4$. We emphasise that in these plots the values of $\bar{u}_k$ and $\bar{T}_k$ are outputs of the model, which are in excellent agreement with the predicted value by DNS data.

We then report the relative percentage error in the prediction of wall-shear stress ϵ_{τ_w} and heat flux ϵ_{q_w} for both matching locations in table 6. For the first matching location, $y_m^+ = 150$, the model performs remarkably well at $M_\infty = 2$, with errors in τ_w below 6 % for both M2A and M2I, and an error in q_w of approximately 7 % for case M2I. At $M_\infty = 4$, case M4A shows a comparable error in τ_w of approximately 6 %, while case M4I exhibits a larger error of approximately 16 % in τ_w and 36 % in q_w. For the second matching location, $y_m^+ = 300$, both cases at $M_\infty = 2$ show errors below 15 % in both τ_w and q_w, reflecting the good agreement observed for velocity and temperature profiles in panels (*a*–*b*) of figure 9. Cases at $M_\infty = 4$ show an increase in errors, with τ_w errors reaching approximately 19 % for M4A and 30 % for M4I, and q_w error rising to nearly 48 % for M4I. Comparing the two matching locations, the results reveal a clear trend: the lower matching location $y_m^+ = 150$ generally yields smaller errors in wall-flux predictions across all cases. This improvement is particularly pronounced for the $M_\infty = 4$ cases, where errors roughly double when moving from $y_m^+ = 150$ to $y_m^+ = 300$. The trend is consistent with the expectation that matching closer to the wall, while still remaining above the roughness

https://doi.org/10.1017/jfm.2026.11842 Published online by Cambridge University Press

Case	$y_m^+ = 150$		$y_m^+ = 300$	
	ϵ_{τ_w} [%]	ϵ_{q_w} [%]	ϵ_{τ_w} [%]	ϵ_{q_w} [%]
M2A	−5.84	—	5.15	—
M2I	−2.06	7.10	7.84	14.30
M4A	5.87	—	18.91	—
M4I	15.72	35.67	29.63	47.81

Table 6. *A priori* errors obtained with the present formulation of the wall model using matching locations $y_m^+ = 150$ and $y_m^+ = 300$. The relative errors in the wall-shear stress and heat flux are defined as $\epsilon_{\tau_w} = (\tau_{w,model} - \tau_{w,DNS})/\tau_{w,DNS} \times 100$ and $\epsilon_{q_w} = (q_{w,model} - q_{w,DNS})/q_{w,DNS} \times 100$.

sublayer, reduces the accumulated modelling error in integrating the governing equations from the matching location down to the wall. We attribute the higher errors observed at $M_\infty = 4$, and particularly for case M4I, mainly to inaccuracies introduced from the Van Driest (1951) velocity transformation, which stands out in figure 8 for not being able to perfectly collapse this case onto the subsonic reference as well as the others. This limitation becomes more consequential at higher Mach numbers, where compressibility effects are more significant. An additional assessment of the performance of the model for a different topography consisting of staggered cubical arrays can be found in Appendix B.

8. Conclusions

In this study, we have investigated the validity of the RA for compressible turbulent BLs over prism-shaped roughness using DNSs at Mach numbers 2 and 4, with both adiabatic and isothermal-wall conditions.

Our primary finding is that while surface roughness disrupts the near-wall momentum–energy coupling within the roughness sublayer, the RA recovers its validity outside the roughness sublayer, i.e. 2–3 times the roughness element height. Above the roughness crest, the enthalpy and velocity fields exhibit smooth-wall-like similarity, and the parabolic temperature–velocity relation holds asymptotically. The roughness influence manifests through modified effective boundary conditions rather than through breakdown of the fundamental analogy structure, validating the Townsend outer-layer similarity hypothesis extended to thermal fields in compressible flows.

We have systematically compared three RA formulations (Walz 1969; Huang & Coleman 1994; Zhang *et al.* 2014) against our DNS database. The Huang & Coleman (1994) formulation demonstrates superior consistency between the parabolic fit and near-wall gradients. This suggests that embedding both viscous and turbulent physics within a mixed Prandtl number may be preferable to strictly separating inner and outer constraints.

For the velocity field, the Van Driest (1951) transformation successfully recovers a good degree of outer-layer similarity, collapsing both smooth- and rough-wall compressible profiles onto incompressible counterparts. This enables application of the extensive incompressible rough-wall-modelling framework to compressible flows through appropriate transformations.

Building on these insights, we have developed a physics-based wall model for small roughness ($k \ll \delta$) coupling: (i) the drag-predictive method of Yang *et al.* (2016) with explicit sheltering mechanisms; (ii) the Van Driest (1951) transformation accounting for compressibility effects; and (iii) the Huang & Coleman (1994) RA closure for temperature–velocity coupling. The model predicts both τ_w and q_w from knowledge of

https://doi.org/10.1017/jfm.2026.11842 Published online by Cambridge University Press

the roughness pattern and outer-layer information alone, avoiding resolution of complex roughness-sublayer physics.

A priori testing demonstrates excellent performance at Mach 2, with errors below 8 % for τ_w and 15 % for q_w across both matching locations. At Mach 4, errors increase with the matching height, with τ_w predictions reaching up to 30 % at $y_m^+ = 300$; the larger heat-flux errors are largely a consequence of the degraded drag prediction, rather than a failure of the proposed RA itself, which remains consistent with the velocity transformation accuracy.

Future works are needed to investigate different flow conditions, as well as specific sets of roughness geometries, which may introduce stronger compressibility effects. To this end, we underline that the building blocks of the proposed model rely on physics-based assumptions, such that individual components can be modified to accommodate realistic roughness geometries and more advanced compressibility transformations, while requiring substantially fewer tuneable parameters than traditional semi-empirical correlations.

Future investigations will also consider the implementation of the present framework within wall-modelled large-eddy simulations, enabling *a posteriori* assessments of the model performance in realistic simulation environments.

Acknowledgements. We acknowledge that the results reported in this paper have been achieved using the EuroHPC JU Extreme Scale Access Infrastructure resource Marenostrum 5 hosted at BSC-CNS, Barcelona, Spain, under project EHPC-EXT-2023E01-034. We also acknowledge the CINECA award under the ISCRA and EuroHPC initiatives (project EUHPC_E02_044), for the availability of high-performance computing resources on Leonardo booster. We acknowledge EuroHPC JU for awarding the project ID EHPC-EXT-2024E02-048 access to LUMI at CSC, Finland.

Funding. We acknowledge financial support under the National Recovery and Resilience Plan (NRRP), Mission 4, Component 2, Investment 1.1, Call for tender No. 104 published on 2.2.2022 by the Italian Ministry of University and Research (MUR), funded by the European Union – NextGenerationEU– Project Title ADMIRE – CUP B53C24006770006 – Grant Assignment Decree No. 1401 adopted on 18/09/2024 by the Italian Ministry of Ministry of University and Research (MUR). This research received also financial support from ICSC – Centro Nazionale di Ricerca in 'High Performance Computing, Big Data and Quantum Computing', funded by European Union – NextGenerationEU.

Data availability statement. The data that support the findings of this study are available upon reasonable request. Python code implementing the proposed model is available in the following public repository: https://github.com/cogomichele/cogo2026-wall-model.git.

Declaration of interests. The authors report no conflict of interest.

Appendix A

Yang *et al.* 2016 showed that the streamwise mean velocity profile resembles an exponential function (6.1) of the wall-normal coordinate for a good portion of the region between the wall and the roughness crests. This approach is based on the von Kármán–Pohlhausen integral method, in which a shape function is assumed for the mean velocity profile $\bar{u}(y)$ and its parameters are determined based on momentum conservation and considerations about the topography of the roughness pattern.

To fully characterise the profiles described in (6.1), and (6.2), five parameters are required: u_k, u_τ, d, z_0, a, while information on the matching location $\bar{u}_m$, roughness height k and the geometrical distribution of the roughness elements are known. These 5 unknowns need 5 constraints: one can be found by using the momentum balance and two from continuity of the velocity profile. A fourth fundamental constraint is obtained by the relation between the displacement height d and the centre of force. The fifth constraint determines the attenuation coefficient a of the exponential profile and is based on considerations about the sheltering mechanism.

https://doi.org/10.1017/jfm.2026.11842 Published online by Cambridge University Press

The first is obtained by vertical integration of the momentum balance between the downward momentum flux within the inertial layer and the form drag due to roughness

$$A_T u_\tau^2 = \int_{A_f} C_d \bar{u}(y)^2 \, \mathrm{d}A_f. \tag{A1}$$

This is possible because of the fully rough regime assumption, which allows us to neglect the viscous terms in the balance. Substituting (6.1) in (A1) and integrating from $y = 0$ to $y = k$, assuming $C_d = 1$, the relation for rectangular prism roughness elements becomes

$$u_\tau^2 = \frac{1 - e^{-2a}}{2a} \lambda_f C_d \bar{u}_k^2, \tag{A2}$$

where $\lambda_f = A_f / A_T$ is the frontal solidity, and A_f and A_T are the projected frontal and horizontal lot areas, respectively. The second condition is related to the continuity of the velocity profile imposed at $y = k$, which results in (6.3).

The third constraint is the continuity at the matching location of choice $y = y_m$. This equation is posed in an integral form, since the velocity profile is modified by density variations along the log-layer. By equating the integral of (6.2) and $\bar{u}_m$

$$\int_{y=k}^{y=y_m} \frac{\mathrm{d}\bar{u}}{\mathrm{d}y} \, \mathrm{d}y = \bar{u}_m - \bar{u}_k = \int_{y=k}^{y=y_m} \frac{u_\tau}{k} \frac{1}{y - d} \sqrt{\frac{\bar{\rho}_w}{\bar{\rho}}} \, \mathrm{d}y. \tag{A3}$$

The displacement height d is set to be equal to the centroid height of the distributed drag force, that is,

$$d = \frac{\int_{A_f} C_d \bar{u}(y)^2 y \, \mathrm{d}A_f}{\int_{A_f} C_d \bar{u}(y)^2 \, \mathrm{d}A_f}. \tag{A4}$$

Again, cubical roughness, substituting the exponential profile from (6.1) and integrating from $y = 0$ and $y = k$, (A4) simply leads to

$$\frac{d}{k} = \frac{1}{1 - e^{-2a}} - \frac{1}{2a}. \tag{A5}$$

Combining equations (A1), (6.3) and (A5), an expression for z_0 is soon obtained

$$\frac{z_0}{k} = \left(1 - \frac{d}{k}\right) exp\left[\frac{-\kappa}{\sqrt{\frac{1}{2a} C_d \lambda_f (1 - e^{-2a})}}\right]. \tag{A6}$$

The influence of the surface topography is evaluated as a series of steps to estimate the ratio between the friction velocity u_τ and the mean velocity at the crest of the roughness $\bar{u}_k$. First, an initial guess of $u_\tau / \bar{u}_k$ (e.g. 0.1) is used to evaluate the sheltering height h_s, applying the expression

$$h_s = max[k - c_\theta (u_\tau / \bar{u}_k) L_x; 0], \tag{A7}$$

where c_θ is a wake expansion coefficient equal to unity for cubical elements, while L_x is the spacing between elements in the streamwise direction. Then, the attenuation factor is obtained by writing the momentum balance, considering the sheltered portion of the downstream cube, which gives

https://doi.org/10.1017/jfm.2026.11842 Published online by Cambridge University Press

$$a = \frac{a_{min}}{1 - h_s/h}, \tag{A8}$$

where $a_{min} \simeq 0.4$ for unsheltered cases. Now, we can calculate d and y_0 using (A5) and (A6), respectively. Finally, we obtain the corrected u_τ/U_h with (6.3) and iterate until convergence.

At the end of this process, an initial guess of u_τ and is chosen and the differential logarithmic layer is integrated from $y = k$ up to the matching location y_m. The convergence of u_τ is verified by the equivalence of the integrated velocity profile at y_m with the u_m from DNSs.

Appendix B

In this section, we test the accuracy of the present model in the case of a boundary-layer flow at $M_\infty = 2$, occurring over staggered cubical arrays under adiabatic wall conditions, using data from the CB_S case of Cogo *et al.* (2025*b*). This analysis allows for an evaluation of the momentum–energy coupling in the present model on a different roughness geometry, however, the adiabatic condition at the wall prevents a direct assessment of the heat flux. Following the approach of Yang *et al.* (2016), the evaluation of the sheltered height h_s differs for this topographical configuration compared with the aligned case analysed in Appendix A. For staggered arrays, wake interactions between roughness elements may involve both the streamwise and spanwise directions. Based on the flow condition and the value of frontal solidity, the sheltering for a particular cube may be due to the element directly upstream and possibly the two elements located upstream left and upstream right. Yang *et al.* (2016) provided an analytical method to decompose these contributions for the case of cubical roughness. The heights of the sheltered regions due to the upstream cube and the upstream-lateral cubes are, respectively,

$$h_1 = max\left(0, k - L_x \frac{u_\tau}{\bar{u}_k}\right) \tag{B1}$$

and

$$h_2 = max\left(0, k - \frac{u_\tau}{\bar{u}_k}(L_x - k)/2\right). \tag{B2}$$

The spanwise extension of the sheltered regions due to the upstream-lateral cubes is

$$w_2 = max\left(0, \frac{u_\tau}{\bar{u}_k}(L_x - k)/2 - (L_y - k)/2\right), \tag{B3}$$

where L_y is the spanwise distance between the lateral elements. Finally, the total sheltered area is

$$A_s = (k - 2w_2)h_1 + 2w_2 h_2 \tag{B4}$$

and we can calculate the sheltered height with

$$h_s = A_s/k. \tag{B5}$$

Figure 10 shows the performance of the model in comparison with the DNS data of Cogo *et al.* (2025*b*) for staggered arrangements. Results from case M2A (aligned cubes) are also reported for reference. The coupling of the sheltering model of Yang *et al.* (2016), with the compressible transformation of Van Driest (1951), produces an accurate prediction of both mean rescaled velocity and temperature profiles, even for this geometrical arrangement, confirming the ability of the sheltering model to provide a reliable estimate of the

https://doi.org/10.1017/jfm.2026.11842 Published online by Cambridge University Press

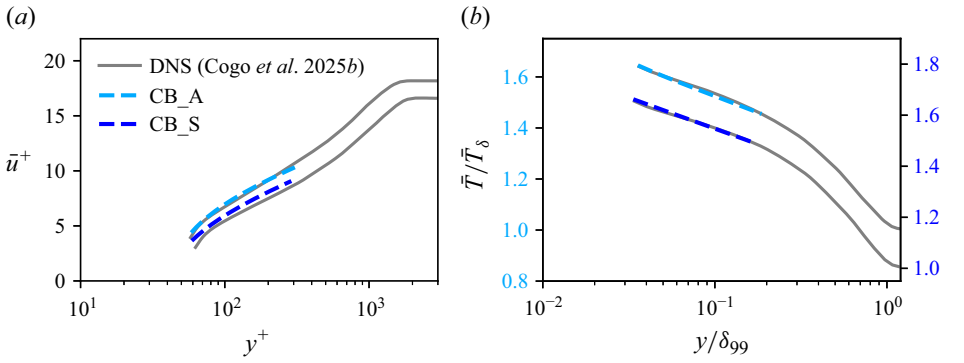


Figure 10. Mean rescaled velocity (*a*) and temperature (*b*) profiles as function of the wall-normal coordinate y^+ and y/δ_{99}, respectively, for both the aligned (CB_A) and staggered (CB_S) roughness types. Both cases share the same Mach number $M_\infty = 2$ and adiabatic wall (Cogo *et al.* 2025*b*). Results for CB_A and the respective reference DNS data are manually shifted upwards by $\Delta T = 0.15$ in panel (*b*). The matching location for both cases is located at $y_m^+ = 300$.

ratio $u_\tau/\bar{u}_k$ from this topography and of the Van Driest transformation to account for density variation in the log layer. The *a priori* relative errors in the prediction of τ_w remain confined within 13 % for both matching locations considered: $\epsilon_{\tau_w} = -12.48$ % at $y_m^+ = 150$ and $\epsilon_{\tau_w} = -8.16$ % at $y_m^+ = 300$. The error in the prediction of q_w is not reported for adiabatic wall cases.

References

Bernardini, M., Modesti, D., Salvadore, F., Sathyanarayana, S., Della Posta, G. & Pirozzoli, S. 2023 STREAmS-2.0: supersonic turbulent accelerated Navier–Stokes solver version 2.0. *Comput. Phys. Commun.* **285**, 108644.

Bons, J. 2005 A critical assessment of Reynolds analogy for turbine flows. *J. Heat Transfer* **127** (5), 472–485.

Bowersox, R. 2007 Survey of high-speed rough wall boundary layers: invited presentation. In *37th AIAA Fluid Dynamics Conference and Exhibit*, *AIAA Paper* 2007–3998.

Busemann, A. 1931 *Gasdynamik*. Akademische Verlagsgesellschaft.

Chaudhuri, A., Hadjadj, A., Chinnayya, A. 2011 On the use of immersed boundary methods for shock/obstacle interactions. *J. Comput. Phys.* **230** (5), 1731–1748.

Chen, K.C. 1972 Compressible turbulent boundary-layer heat transfer to rough surfaces in pressure gradient. *AIAA J.* **10** (5), 623–629.

Chung, D., Hutchins, N., Schultz, M.P. & Flack, K.A. 2021 Predicting the drag of rough surfaces. *Annu. Rev. Fluid Mech.* **53**, 439–471.

Cogo, M., Baù, U., Chinappi, M., Bernardini, M. & Picano, F. 2023 Assessment of heat transfer and Mach number effects on high-speed turbulent boundary layers. *J. Fluid Mech.* **974**, A10.

Cogo, M., Modesti, D., Bernardini, M. & Picano, F. 2025*a* Surface roughness effects on subsonic and supersonic turbulent boundary layers. *J. Fluid Mech.* **1009**, A56.

Cogo, M., Modesti, D., Picano, F. & Bernardini, M. 2025*a* Development of supersonic turbulent boundary layers over prism-shaped rough surfaces. *J. Fluid Mech.* **1025**, A21.

Crocco, L. 1932 Sulla trasmissione del calore da una lamina piana a un fluido scorrente ad alta velocità. *L'Aerotecnica* **12**, 181–197.

De Vanna, F., Benato, A., Picano, F. & Benini, E. 2021 High-order conservative formulation of viscous terms for variable viscosity flows. *Acta Mech.* **232**, 2115–2133.

Ducros, F., Ferrand, V., Nicoud, F., Weber, C., Darracq, D., Gacherieu, C. & Poinsot, T. 1999 Large-eddy simulation of the shock/turbulence interaction. *J. Comput. Phys.* **152** (2), 517–549.

Griffin, K.P., Fu, L. & Moin, P. 2021 Velocity transformation for compressible wall-bounded turbulent flows with and without heat transfer. *Proc. Natl Acad. Sci. USA* **118** (34), e2111144118.

Hasan, A.M., Larsson, J., Pirozzoli, S. & Pecnik, R. 2023 Incorporating intrinsic compressibility effects in velocity transformations for wall-bounded turbulent flows. *Phys. Rev. Fluids* **8** (11), L112601.

https://doi.org/10.1017/jfm.2026.11842 Published online by Cambridge University Press

HILL, J., VOISINET, R. & WAGNER, D. 1980 Measurements of surface roughness effects on the heat transfer to slender cones at Mach 10. In *18th Aerospace Sciences Meeting*, *AIAA Paper* 1980-0345.

HUANG, P.G. & COLEMAN, G.N. 1994 Van Driest transformation and compressible wall-bounded flows. *AIAA J.* **32** (10), 2110–2113.

HUANG, J., DUAN, L. & CHOUDHARI, M.M. 2022 Direct numerical simulation of hypersonic turbulent boundary layers: effect of spatial evolution and Reynolds number. *J. Fluid Mech.* **937**, A3.

JIMÉNEZ, J. 2004 Turbulent flows over rough walls. *Annu. Rev. Fluid Mech.* **36**, 173–196.

LARSSON, J. & PIROZZOLI, S. 2026 Wall-bounded turbulence. In *Turbulence and Transition in Supersonic and Hypersonic Flows, Computation and Analysis of Turbulent Flows* (ed. J. Larsson & X. Zhong), pp. 387–452. Academic Press.

MODESTI, D., SATHYANARAYANA, S., SALVADORE, F. & BERNARDINI, M. 2022 Direct numerical simulation of supersonic turbulent flows over rough surfaces. *J. Fluid Mech.* **942**, A44.

OWEN, P.R. & THOMSON, W.R. 1963 Heat transfer across rough surfaces. *J. Fluid Mech.* **15** (3), 321–334.

PELTIER, S.J., HUMBLE, R.A. & BOWERSOX, R. 2016 Crosshatch roughness distortions on a hypersonic turbulent boundary layer. *Phys. Fluids* **28** (4), 045105.

ROUHI, A., CHUNG, D. & HUTCHINS, N. 2019 Direct numerical simulation of open-channel flow over smooth-to-rough and rough-to-smooth step changes. *J. Fluid Mech.* **866**, 450–486.

SATHYANARAYANA, S., BERNARDINI, M., MODESTI, D., PIROZZOLI, S. & SALVADORE, F. 2025 High-speed turbulent flows towards the exascale: STREAmS-2 porting and performance. *J. Parallel Distrib. Comput.* **196**, 104993.

TOWNSEND, A.A.R. 1980 *The Structure of Turbulent Shear Flow*. Cambridge University Press.

TRETTEL, A. & LARSSON, J. 2016 Mean velocity scaling for compressible wall turbulence with heat transfer. *Phys. Fluids* **28** (2), 026102.

VAN DRIEST, E.R. 1951 Turbulent boundary layer in compressible fluids. *J. Aeronaut. Sci.* **18** (3), 145–160.

WALZ, A. 1969 *Boundary Layers of Flow and Temperature*. MIT Press.

WENZEL, C., GIBIS, T. & KLOKER, M. 2022 About the influences of compressibility, heat transfer and pressure gradients in compressible turbulent boundary layers. *J. Fluid Mech.* **930**, A1.

WILLIAMS, O.J.H., SAHOO, D., PAPAGEORGE, M. & SMITS, A.J. 2021 Effects of roughness on a turbulent boundary layer in hypersonic flow. *Exp. Fluids* **62**, 1–13.

YANG, X.I.A., SADIQUE, J., MITTAL, R. & MENEVEAU, C. 2016 Exponential roughness layer and analytical model for turbulent boundary layer flow over rectangular-prism roughness elements. *J. Fluid Mech.* **789**, 127–165.

ZHANG, Y.S., BI, W.T., HUSSAIN, F. & SHE, Z.S. 2014 A generalized Reynolds analogy for compressible wall-bounded turbulent flows. *J. Fluid Mech.* **739**, 392–420.

ZHANG, C., DUAN, L. & CHOUDHARI, M.M. 2018 Direct numerical simulation database for supersonic and hypersonic turbulent boundary layers. *AIAA J.* **56** (11), 4297–4311.

https://doi.org/10.1017/jfm.2026.11842 Published online by Cambridge University Press